Soft Matter

Accepted Manuscript

ROYAL SOCIETY OF CHEMISTRY

www.rsc.org/softmatter

ARTICLE TYPE www. rsc.org/xxxxxx | XXXXXXXX

Microfluidic processing of concentrated surfactant mixtures: online SAXS, microscopy and rheology

Hazel P. Martin,[a‡] Nicholas J. Brooks,[b] John M. Seddon,[b] Paul F. Luckham,[a] Nick J. Terrill,[c] Adam J. Kowalski,[d] and João T. Cabral[a*]

Received Xth XXXXXXXXXX 20XX, Accepted Xth XXXXXXXXX 20XX
First published on the web Xth XXXXXXXXXX 200X
DOI: 10.1039/b000000x

We investigate the effect of microfluidic flow on the microstructure and dynamics of a model surfactant mixture, combining synchrotron Small Angle X-ray Scattering (SAXS), microscopy and rheology. A system comprising a single-chain cationic surfactant, hexadecyl trimethyl ammonium chloride (C_{16}TAC), a short-chain alcohol (1-pentanol) and water was selected for the study due to its flow responsiveness and industrial relevance. Model flow fields, including sequential contraction-expansion (extensional) and rotational flows, were investigated and the fluid response in terms of the lamellar *d*-spacing, orientation and birefringence was monitored *in situ*, as well as the recovery processes after cessation of flow. Extensional flows are found to result in considerable *d*-spacing increase (from approx 59 Å to 65 Å). However, under continuous flow, swelling decreases with increasing flow velocity, eventually approaching the equilibrium values at velocities $\simeq$2 cms^{-1}. Through individual constrictions we observe the alignment of lamellae along the flow velocity, accompanied by increasing birefringence, followed by an orientation flip whereby lamellae exit perpendicularly to the flow direction. The resulting microstructures are mapped quantitatively onto the flow field in 2D with 200 μm spatial resolution. Rotational flows alone do not result in appreciable changes in lamellar spacing and flow type and magnitude evidently impact the fluid microstructure under flow, as well as upon relaxation. The findings are correlated with rheological properties measured *ex-situ* to provide a mechanistic understanding of the effect of flow imposed by tubular processing units in the phase behavior and performance of a model surfactant system with ubiquitous applications in personal care and coatings industries.

1 Introduction

Surfactant molecules in solution self-assemble to form thermodynamically stable microstructures, often referred to as lyotropic liquid crystalline phases.[1–3] The morphology and stability of the phases formed depend highly on the shear flow history experienced during processing, and generally combines various degrees of extension and rotation. The magnitude and type of shear applied largely determines the characteristic phases formed by the surfactant systems during and after processing, reaching a pseudo-equilibrium state upon relaxation.[4–6] The effect of shear on surfactant mixtures has therefore been the focus of numerous studies aimed at understanding the dynamics and nonequilibrium behaviour of self-assembled amphiphilic molecules, of great interest to applications ranging from personal care, foods, paints and other coating products.[2,3]

Surfactant mixtures, containing surface active agents such as the ubiquitous cationic surfactant hexadecyl trimethyl ammonium bromide (C_{16}TAB) or sodium dodecyl sulfate (SDS), are known to exhibit remarkable response under flow, associated to their equilibrium and non-equilibrium microstructural behaviour.[5–10] In the present work, we study the influence of model flow fields on the microstructure and relaxation of a surfactant mixture in microdevices. The microfluidic environment offers precise control of the magnitude and geometry of the flow fields[11–16] and may be combined with online synchrotron Small Angle X-ray Scattering (SAXS) to follow changes in the lyotropic phases under flow. Despite the challenges of coupling X-ray scattering with microdevices, due to material compatiblity and scattering background,[17,18] successful experiments have been carried out, including the resolution of ms-conformational changes in proteins and RNA,[19–21] alignment of anisotropic particles and liquid crystals,[22,23] phase transitions in block copolymer solutions[24] The structural changes in the spatially varying flows, analogous to the processing and manufacturing routes in a tubular reactor, can be correlated with the vis-

[a] *Department of Chemical Engineering, Imperial College London, London SW7 2AZ, UK. E-mail: j.cabral@imperial.ac.uk*
[‡] *Current address: European Patent Office, Patentlaan 2, 2288 EE Rijswijk, The Netherlands*
[b] *Department of Chemistry, Imperial College London, London SW7 2AZ, UK.*
[c] *Diamond Light Source, Harwell Science and Innovation Campus, Oxfordshire, OX11 0DE, UK.*
[d] *Unilever Research & Development, Port Sunlight, Bebington CH63 3JW, UK.*

coelastic properties of the complex fluid to elucidate the interplay of flow history and rheological properties of polymer solutions[19,20,25] and surfactant mixtures.[26–31] This microfluidic approach is thus complementary to well-established rheo-SAXS and stopped-flow techniques,[4,32] providing unprecedented spatio-temporal insight into the flow response of complex fluids.

2 Materials and methods

2.1 Materials

The system studied comprises a single-chain cationic surfactant, a short-chain alcohol and water. Hexadecyl trimethyl ammonium chloride (C_{16}TAC, viz. $C_{19}H_{42}ClN$) and 1-pentanol (C_5OH, viz. $C_5H_{12}O$), were obtained from Sigma-Aldrich and the continuous phase was deionised, membrane-purified water (Elga Option 4 water purifier). Pentanol exhibits low water solubility, at approximately 22g/L. Ternary systems of CTAB (hexadecyl-trimethyl-ammonium bromide)/alcohol/water have been studied extensively and the phase diagrams mapped in detail,[33,34] providing useful analogs to CTAC phase behaviour. The ternary system of 17.4 wt% C_{16}TAC, 20 wt% C_5OH and 62.6% H_2O, self-assembles into a lamellar L_α mixed phase (with excess water) at equilibrium, as shown below (although wormlike micelles are well-known to form in aqueous CTAC solutions in the presence of salt[35]). The solution was mixed vigorously for 2 minutes at room temperature and the sample was stored for 72 hours.

2.2 Methods

2.2.1 Microflow processing. Microdevice fabrication involved the circuit design on a CAD programme, high resolution printing onto an acetate photomask and SU8 photolithography to prepare a master. Figure 1 depicts selected microchannel geometries investigated. A modified rapid prototyping approach by soft lithography was employed to fabricate the microfluidic chip, building upon well-established methods.[16,36–39] A thin (1-2 mm) polydimethyl siloxane (PDMS) replica membrane of the microchannel was reinforced by a second PDMS block around the inlet, outlet and sides of the device. This mm-thick PDMS membrane is required to keep SAXS background relatively low,[18] as shown in Fig 3b, while retaining structural integrity of the device and reducing flow-induced deformation of the microchannels.[40] The PDMS reinforcing matrix was moulded around a plasma-glassified piece of PDMS positioned over the microchannels, which is removed once the walls are formed. After punching in- and outlets, the PDMS stamp is irreversibly sealed to a glass slide using plasma oxidation.

Microfluidic devices with channels of 70 µm in height, width varying from 100 to 2000 µm and 16 cm in overall length were fabricated. The first section of the microchannel, labeled 'processing' section (*cf.* Fig. 1), was designed to confer selected flow field types over a total length of 3 cm and maximum width 1000 µm. Four different types of flow fields were investigated and are depicted in Fig. 1. A reference chip, labelled **MC1** was used as a basis for comparison, imposing flow through a straight channel. The geometry labelled **MC2** corresponds to a sequential extensional flow field imposed by four constrictions of 100 μm width and 820 μm long with angle approximately 60°. The additional flow types studied are a flow field combining both extension and rotation in microfluidic chip **MC3** by means of circular posts in a hexag-

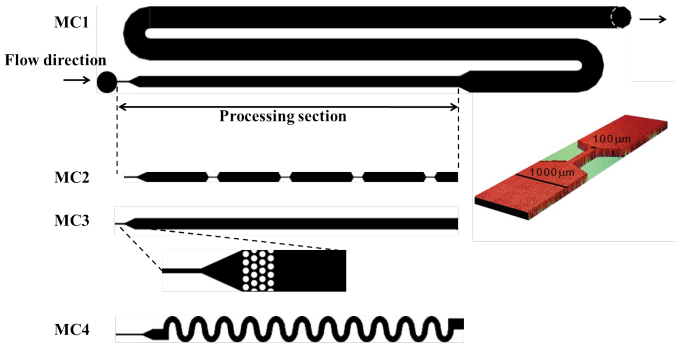

Fig. 1 Microfluidic channel designs: reference **MC1** comprises an unpatterned 'processing' section, 3cm long and 1000 µm wide channel, followed by remaining 13 cm of channel with a width of 2000 µm; the processing section of **MC2** comprises a series of four constrictions with minimum width of 100 µm and a length of 820 µm; **MC3** comprises an array (5 x 4) of circular posts with diameter of 150 µm and inter-post spacing of 50 µm; the processing section of **MC4** comprises 22 bends with outside diameter of 1750 µm, forming a total average flow path length of 13.8 mm.

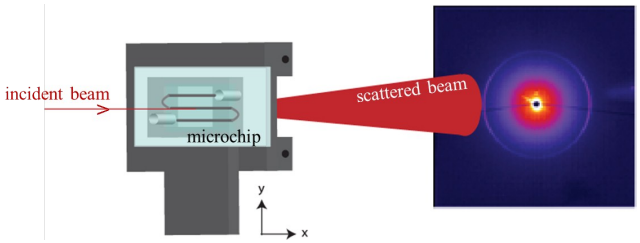

Fig. 2 Schematic of experimental online SAXS setup, depicting the microdevice clamped on an temperature-controlled, XY-motorised stage, and a typical 2-D SAXS pattern. A 150 µm× 150 µm X-ray beam is scanned along the microchannels, within a thin (≃ 1mm) PDMS window, mechanically reinforced by a cm-thick PDMS frame. An array of absorption markers (lead-tape and copper wire) was superposed onto the device to facilitate the establishment of an XY frame of reference and permit accurate SAXS beam scanning along the microchannels.

onal array across the flow and a dominantly rotational flow field in microfluidic chip **MC4**, through a sinusoidal channel. The remaining channel length was designed to observe the response and relaxation following the different flows imposed by the various processing sections. The volumetric flow rates were controlled from 0.1 to 5 mLh^{-1}, corresponding to fluid residence times of approximately 2 - 400 s in the processing section depending also on the flow geometry and of 20 s to 21 min in the total length of the microchannel.

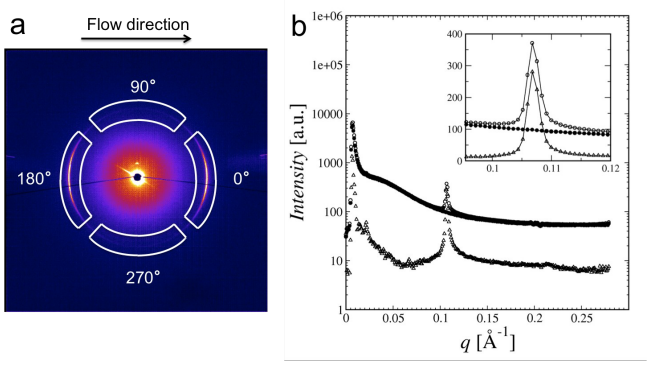

Fig. 3 (a) 2-D SAXS pattern of the system CTAC/Pentanol/Water in microfluidic device with 4 quadrants of azimuthal angles corresponding to parallel (90 and 270°) and perpendicular orientations to the flow direction (b); 1-D SAXS data analysis for background subtraction of the sample (CTAC/Pentanol/Water) measurements in the microfluidic chip: (○) raw 1-D data for the sample in microdevice, (●) 1-D data of PDMS microdevice background, and (▲) 1-D SAXS data of sample following background subtraction; Inset: detail of 1-D SAXS data on characteristic structural peak for the CTAC/Pentanol/Water sample.

2.2.2 Small Angle X ray Scattering. Synchrotron SAXS measurements were carried out at beamline I22, Diamond Light Source (Oxfordshire, UK), with a focused beam of wavelength $\lambda \approx 1.4$ Å (energy $E \approx 8.9$ keV) providing a measurement wavenumber range of $q = 0.0008$ - 0.2788 $Å^{-1}$, where $q = 4\pi/\lambda sin(\theta/2)$ and θ is the scattering angle. The beam cross section was approximately 150×100 μm^2, commensurate with most device features. Both microdevices and holder for the SAXS experiments were custom made as depicted by Fig. 2. The temperature was controlled at 20°C through cartridge heaters in direct contact with the chip holder. Typical acquisition times were 10 s per 2D scattering frame. In order to accurately develop a spatial frame of reference for flow mapping, an array of absorption markers was superimposed onto the glass face of the microdevice, including lead tape segments and thin copper wire. The initial stage of the SAXS experiment required the precise XY mapping of microchannel layout, in order to carry out spatio-temporal flow measurements over many cm, with 100-200 μm illuminated area.

Two major features are obtained from the SAXS data: the orientation of the lamellar sheets and the interlamellar spacing. Figure 3a illustrates a typical 2-D SAXS pattern obtained for the surfactant mixture under flow. The scattering pattern is, in the first instance, subdivided into four symmetric quadrants to quantify the order and orientation of structures according to the azimuthal angle. For structures aligned with the flow, the scattering intensity peaks at azimuthal angles of 90 and 270° and for those aligned perpendicularly to the flow, the intensity peaks at azimuthal angles of 0 and 180°. Centrosymmetric scattering rings characterise isotropic lamellar sheets and deviations quantify their orientation along the flow (perpendicular alignment to the flow is illustrated in Fig. 3a). The data were reduced and analysed with Diamond software package DREAM and a custom program.

2.2.3 Microscopy and Rheology. *In-situ* microscopy measurements were carried out on a reflection optical microscope (Olympus BX41M), equipped with a custom made temperature-controlled XY stage and CCD camera (AVT Marlin). Velocity mapping was accomplished by fluorescent particles (2-15 μm diameter) tracking using an Olympus IX71 fluorescence microscope. Viscoelastic properties were measured *ex-situ* using a cone and plate geometry with a TA Instruments AR-2000 stress-controlled rheometer and a concentric cylinder/couette geometry using either a Haake RS1 stress-controlled rheometer or a Paar Physica UDS200 stress/shear controlled rheometer.

3 Results and discussion

3.1 Contraction-expansion flows

We concentrate first on the structural orientation of the surfactant solution under flow. Figure 4 depicts the combined experimental results obtained by polarised optical microscopy and SAXS, as the system flows through the first of four 'processing' constrictions in **MC2** at a volumetric flow rate of 5 mLh^{-1}, corresponding to a velocity of ≈ 20 cms^{-1} in the constriction. The velocity flow profile of the system was determined by particle tracking and found to be well described by plug flow prior and within constrictions, shown in Fig. 5, enabling simple extension rate computations. This behaviour is expected from the highly shear thinning rheology discussed below. Both wall slip and shear thinning render estimations of wall shear rate rather inaccurate; nevertheless Son's approach[41] was followed to obtain relative estimates. At flow rate of 5 mLh^{-1}, the extension rate during contraction can be geometrically estimated to be 4170 s^{-1} (with wall shear $\simeq$ 8330 s^{-1}).

From the optical micrograph in Fig. 4, the degree of alignment through the constriction and associated orientation

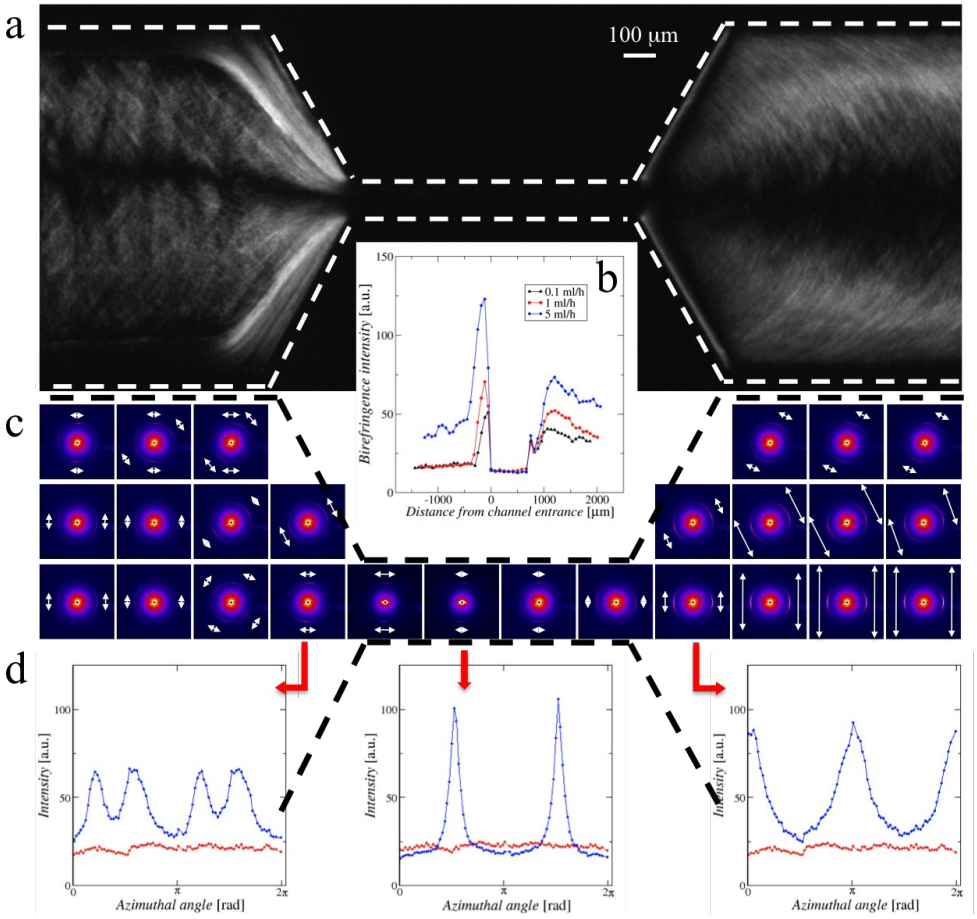

Fig. 4 CTAC/Pentanol/Water system under flow through the first constriction of **MC2** from width of 1000 µm to 100 µm at flow rate 5 mLh^{-1}; a) crossed polarised optical micrograph; b) birefringence intensity along the channel from the constriction entrance; c) 2-D SAXS map; d) azimuthal average of the intensity for 2-D SAXS for surfactant system (○) and for background (●) at constriction entrance (left), within the constriction (middle), and upon exit (right).

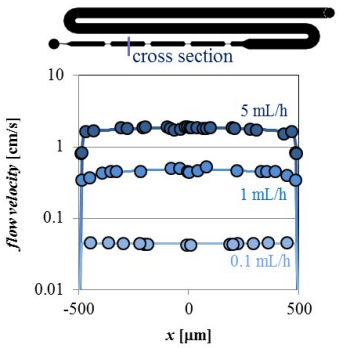

Fig. 5 Cross-sectional flow velocity of CTAC/Pentanol/Water obtained by particle tracking using 2 μm diameter fluorescent particles at three representative flow rates 0.1, 1 and 5 mLh^{-1}, corresponding to an approximate plug flow profile.

changes can be qualitatively estimated. The birefringence is shown to scale with the volumetric flow velocity, for three flow rates (0.1, 1 and 5 mLh^{-1}) shown in Fig. 4b, across the constriction. It increases shortly before the constriction and then nearly vanishes within the narrow channel, before rapidly recovering upon exit. The birefringence intensity correlates with the degree of alignment of the lamellar phase, which is quantified by SAXS at the molecular scale. Examination of the 2-D SAXS patterns in Fig. 4c reveals that, before the constriction, the lamellae structures align with the channel walls and remain mostly isotropic along the channel centreline, separated by a cross-over where multiple orientations coexist. Since the flow is symmetric along the centreline, only half of the microchannel is mapped by focussed SAXS. Evidently, the geometric constriction forces the lamellar stacks to align with the flow upon entrance, then orthogonally to it upon exit, as the fluid decelerates. A quantitative representation of the orientational order is obtained by plotting the scattering intensity around the structural peak as a function of the azimuthal angle, as shown in Fig. 4d. For comparison, the background scattering is superposed onto the surfactant data. At the constriction entrance, an azimuthal scan reveals double scattering peaks at angles 45 and 135°, and 225 and 305° indicating cross-lamellae alignment to constriction walls. Within the narrow constriction, the lamellae peaks narrow around 90 and 270°, along the flow direction. Upon exiting the constriction, the orientation peaks flip to azimuthal angles of 0 and 180°. The intensities of the scattering peaks indicate a significant orientation degree within the narrow constriction, where simultaneously a lack of birefringence is observed under cross polarised microscopy Fig. 4a. Indeed, within the constriction, the lamellar structures are highly aligned parallel to the flow, exhibiting effectively single crystalline order and thus very little birefringence. Upon expansion, the lamellae flip to a perpendicular orientation to the flow and return to a less ordered, 'polycrystalline' arrangement.

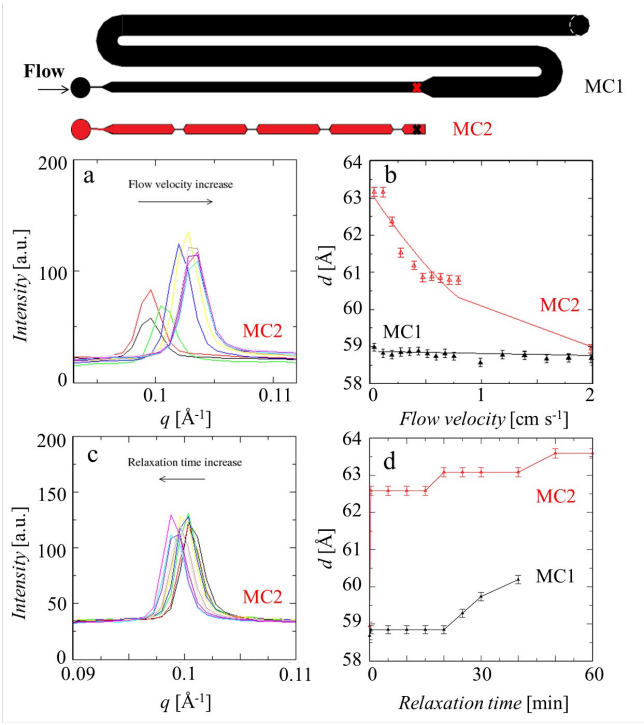

Fig. 6 SAXS measurements for reference flow field (**MC1**) and oscillatory extensional field (**MC2**) of CTAC/Pentanol/Water. All measurements were taken at the same location on the microfluidic chip for both **MC1** and **MC2** as indicated by a red cross on the microchannel schematic. (a) 1-D SAXS data for oscillatory extensional flow, imposed by 4 constrictions with widths consecutively going from 1000 μm to 100 μm (**MC2**) as a function of flow velocities; (b) Computed interlamellar d-spacing following oscillatory extensional flow (△ **MC2**) and in reference flow **MC1** (▲). (c) SAXS data for **MC2** upon cessation of flow, following a rate of 5 mLh^{-1} and (d) corresponding d-spacing for both geometries compared **MC1** and **MC2**.

The change in orientation of the lamellar sheets is accompanied by a variation in the lamellae d-spacing, although this does not happen during transit through a constriction, but rather throughout the 'processing' unit. For comparison, the characteristic interlamellar distance for this system was measured *ex-situ* to be 58.8 Å in quiescent conditions, using a standard mica cell. Figure 6 summarises the kinetics observed for the interlamellar distance upon flow through a straight channel in **MC1**, as a reference for the previously described sequential extensional flow field in **MC2**.

SAXS measurements were performed at the same location within the two microfluidic devices: immediately after the processing section of the microchannel (3 cm from injection), indicated with a marker (×) on the microchannel schematic

in Fig. 6. Both the effect of flow velocity, ranging from 0.04 to 2.0 cms^{-1} (Fig. 6a,b), and the subsequent relaxation behaviour (Fig. 6c,d) were studied. With increasing flow rate in the straight microchannel **MC1**, the d-spacing (obtained from the peak position $d \equiv 2\pi/q^*$) remained largely constant throughout and in accord with the equilibrium value. Therefore, any wall shear present in the straight channel does not appear to affect the lamellar spacing, within measurement uncertainty, at the flow rates investigated. However, significant changes in the spacing were observed under extension with **MC2**: the scattering peak moves from lower q, compared to the quiescent value, and shifts to higher q, corresponding to a decrease in d-spacing, with increasing flow velocity, shown in Fig. 6a. Decreases in d spacing, from the equilibrium value, in L_α systems ($C_{16}E_6/D_2O$) under extensional flow have been reported[42] with increasing extension rate. In our system, however, at low flow rates (approx. 0.1 cms^{-1}), the spacing actually increases up to $\simeq$ 63.3 Å after 'processing'. Further increasing the flow rate drives the lamellar d-spacing to *decrease*, approaching the quiescent value of 58.8 Å for the maximum velocity studied of 2 cms^{-1}. The increase in interlamellar distance is clearly associated with the extensional flow, since it is absent in the 'control' microchannel **MC1**. However, the d-spacing does not correlate simply with real-time changes under flow and must be rationalised in terms of the residence time and structural relaxation after extension.

3.2 Residence time and relaxation upon cessation of extensional flow

At higher flow rates, the fluid experiences larger extension rates but for a shorter time, whereas at lower flow velocities the 'processing' residence time increases. In order to investigate this recovery effect, the structural relaxation was monitored for 1 hour after cessation of flow, following convection at the maximum velocity of 2 cms^{-1} (corresponding to 5 mLh^{-1} rate). For both the simple flow field (**MC1**) and the oscillatory extensional flow field (**MC2**), the spacing between lamellar sheets increased with time, although with different magnitudes. Fig. 6c shows the structural peak shifting to lower q with relaxation time and the corresponding d-spacing is plotted in Fig. 6d for a selected flow rate 5 mLh^{-1}. The 'relaxation' time on the graph is referenced to the moment of cessation of flow and the first actual measurement was acquired at approximately t = 20 s, the operating time plus the 10 s acquisition time. Within this short time frame, a substantial part of this relaxation following processing takes place for the oscillatory extensional flow field, resulting in a rapid d increase from 58.9 to 62.6 Å, followed by a slower increase up to 65 Å during the subsequent hour. By contrast, the d values of samples subjected to (**MC1**) remain unchanged for the first 20 min and then grow gradually to approximately 60 Å indicating that wall shear eventually affects somewhat the microstructure once flow ceases. Further, we note that no scattering peak is detected after 40 minutes of relaxation time for the surfactant mixture flown through the straight channel. This is accompanied by a loss of birefringence under optical microscopy; however, if pressure is manually applied over the channel, creating local shear, birefringence reappears. This is rationalised in terms of the lamellae sheets orientation being parallel to the wider surface of the channel, and thus perpendicular to the incoming X-rays and not detected on this xy plane. This phenomenon also takes place for the fluid undergoing pulsed extensional flow, but at considerably longer times ($\sim$ hours), in agreement with the observations above.

SAXS permits the characterisation of the lamellar geometry in terms of its d spacing, orientation and order; the absence of X-ray contrast between the sample constituents,[43] however, does not allow further insight into how they are partitioned within the lamellar structure. Neutron scattering[42,44,45] with deuterium labelled compounds could provide further insight into the microstructure and such work is underway. The changes in lamellar d-spacing are tentatively rationalised in terms of the incorporation and expulsion of water molecules caused by flow in this mixed CTAC/Pentanol/Water system. Evidently, microflow is promoting an increase, or swelling, of the lamellae spacing upon *relaxation*, i.e. cessation of flow or substantial velocity reduction; this increase in d-spacing is likely to be caused by the intercalation of water molecules between lamellar sheets and increases of up to 6 Å (approximately 10%) corresponding to approximately 2 water molecules, assuming pure water O-O distances. Such changes are of course averaged over the whole sample and are thus gradual with flow rate and recovery time. A decrease in d-spacing indicates water molecules being expelled from between lamellae under compression, caused by the strong extensional flow fields. Indeed, as the flow rate increases, d decreases as shown in Fig. 6b. Upon cessation of flow, the disrupted lamellae structures reorganise over relatively long time scales, of minutes and hours, accompanied by an increase in d. This 'ageing' effect is well-known from industrial processing and typically manifests itself macroscopically by an increase in viscosity over time (corroborated below). The kinetics of swelling and expulsion depend therefore highly on the flow type and magnitude. Indeed, results in Fig. 6b correspond to residence times of 400 s to 2 s (for the lowest and highest flow velocities, respectively) and the fluid subjected to the latter increases rapidly in d within less that 20 s, corresponding to the first measurement in Fig. 6d.

The longer residence times afforded by the lower flow rates permit an increase of the interlamellar distances upon relaxation whilst in the 'processing' region but yields a more modest eventual increase of d upon relaxation. Higher flow rates, in contrast, yield much larger lamellae swelling but only takes

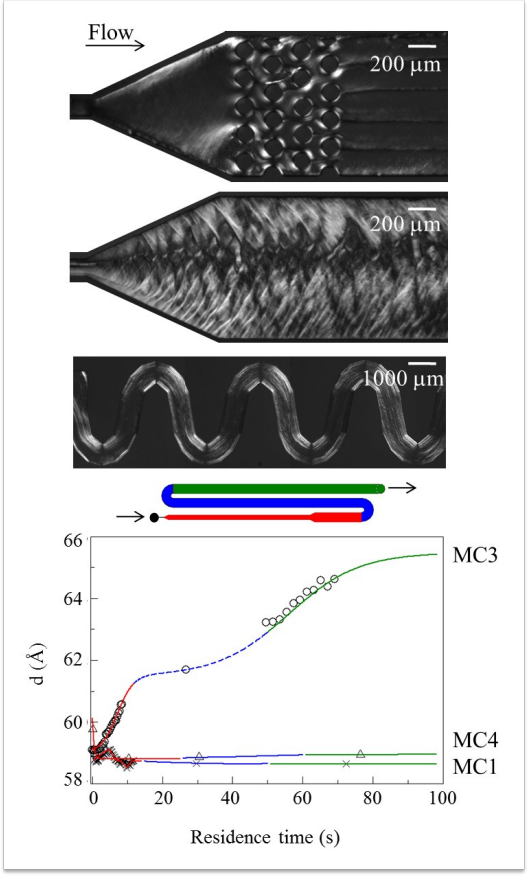

Fig. 7 Structural effect in flow fields with different combinations of extension and rotation at a flow rate of 1mLh^{-1}. *Top*: cross polarised optical micrographs of CTAC/Pentanol/Water in processing section for microflows in **MC1**, **MC3**, and **MC4**; *bottom*: graph comparing the evolution of the lamellar *d*-spacing of the CTAC/Pentanol/Water mixture with flow residence time throughout microfluidic chips **MC1**, **MC3**, and **MC4**.

place upon 'relaxation', which occurs outside the processing section. The fact that the *d*-spacing does not increase through a constriction (travel time $\simeq$5 ms), as shown in Fig. 4, establishes that the incorporation of the water molecules occurs during the reorganisation of the lamellar structure following the extensional flow field, over longer time scales ($\sim$10-100s and beyond).

Both wall shear and large extension rates can, in principle, be responsible for the considerable inter-lamellae swelling observed within **MC2** compared to the straight channel **MC1**. However, comparing the results at *constant* wall shear rate in **MC1** and **MC2**, obtained at different flow rates (*cf.* Fig. 6b), we observe much lower swelling for **MC1** and can therefore conclude that contraction/expansion flows, causing rapid acceleration and deceleration, are largely responsible for swelling. This result is in line with the near plug flow profiles observed (Fig. 5). However, wall shear also appears to be able to cause some *d* increase, albeit at a more modest scale, as shown in the flow relaxation/recovery experiments in Fig. 6d. The interlamellar swelling evidently depends on the type and magnitude of the previously applied shear flow, which determines the water molecule uptake within lamellar sheets upon relaxation.

3.3 Flow type: extensional and rotational flows

To further investigate the effect of flow *type*, scattering from representative flow geometries is compared in Fig. 7. In addition to the reference microchannel **MC1**, we investigated the effect of combined extensional and rotational flow field using microchannel **MC3** and predominantly rotational field in **MC4**. Geometry **MC3** comprises four staggered rows of 5 cylindrical posts with a diameter of 150 µm positioned in a hexagonal array along the flow path, depicted in the optical micrograph of Fig. 7(top). This pattern covers less than 1 mm of the 30 mm long 'processing' unit. Each row of posts imposes contraction-expansion flows and the staggering of consecutive rows further imposes a rotational field. With a flow rate of 1 mLh^{-1}, the fluid experiences a maximum velocity of approximately 4 cms^{-1} and an extension rate of 4170 s^{-1} (estimated maximum wall shear rate of 670 s^{-1}) in contrast to respectively 0.6 cms^{-1} and no extension (approx. wall shear of 170 s^{-1}) in the post-free reference microchannel **MC1**. Both birefringence and lamellar *d*-spacing results are summarised in Fig 7. The cross polarised optical images show, as expected, higher birefringence around the posts where the flow changes direction and accelerates (or decelerates upon exit), as well as birefringence extinction at the cylinder stagnation points (leading and trailing edges), where the fluid is brought to rest, ensued by a downstream streak exhibiting no birefringence and separating five co-flowing steams. The most significant result from geometry **MC3** is the large change in the inter-lamellar distance over time. We compare the *d*-spacing evolution when the CTAC/pentanol/water system is convected through these representative microchannel geometries, in steady state with flow rate 1 mLh^{-1}. While the *d*-spacing remains relatively constant throughout the microchannel **MC1** in the absence of cylindrical posts, the lamellae of the system subjected to extension-rotational flow in **MC3** increase in *d*-spacing from approximately 59 Å to 65 Å over 130 mm of microchannel length, corresponding to a residence time of nearly 100 s. We interpret this increase in terms of an intake of water molecules, swelling the inter-lamellar spacing and, as for **MC2**, we find that this increase does not happen within the active 'processing' region ($<$ 1mm long) but rather over a much longer time (10's of min). Further, according to Fig 7 this increase is not linear in time, as two stages can

be identified in the time-dependence of d. Additional work would be necessary to extract quantitative kinetics and a precise mechanism for this swelling process.

The steady-state flow scan of microchannel **MC1** reveals a small increase ($\simeq$0.3 Å) and decay of d-spacing within the first 8 s residence time, likely caused by the inevitable velocity gradient upon fluid injection into microdevices, depicted in Fig. 1.

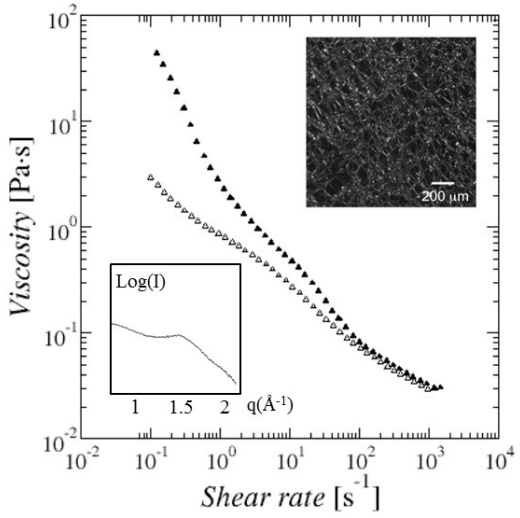

Fig. 8 Flow profile of CTAC/Pentanol/Water with increasing shear rate from 0.1 to 1500 s^{-1} in 4 minutes (▲) and with decreasing shear rate back down to 0.1 s^{-1} in 8 minutes (△); Upper inset: equilibrated cross polarised optical micrograph of CTAC/Pentanol/Water at room temperature; Lower inset: corresponding WAXS data, exhibiting a broad peak (≈1.5 Å), expected for a lamellar L_α phase.

In order to investigate the effect of rotational flow in the lamellar structure, we next report on microchannel geometry **MC4**. A purely rotational flow would require a geometry incompatible with a tubular reactor, like that of a four-roll mill,[12] so rotations (of alternating direction) are introduced by a sinusoidal channel of constant cross-section. The geometry naturally imposes some modest shear, due to the velocity gradient around the channel bends. The crossed polarised optical micrographs, shown in Fig. 7, indicate that birefringent streaks follow the flow direction, accompanying the microchannel contours, showing that the lamellae are oriented with the flow, which is further confirmed by SAXS. We find that the lamellar spacing does not change significantly over time, behaving similarly to reference geometry **MC1** (as both have constant channel cross-section), as shown in Fig 7. These results indicate that, for the flow types and magnitude investigated, the rotational component alone does not cause the lamellae rearrangement associated with increases in d-spacing, corroborating that the latter is mainly caused by extensional flow.

3.4 Impact on rheology

The flow-induced changes of CTAC/pentanol/water system microstructure, as probed by SAXS and microscopy, are accompanied by considerable macroscopic changes in rheology of the solutions. Understanding the interplay between these and the effects of flow is key to engineering and optimising manufacturing processes. This surfactant mixture shear thins and is thixotropic as shown in Fig. 8, measured using a cone and plate geometry. The inset of the figure shows a typical optical micrograph of the quiescent system, characteristic of a lamellar phase. Shear recovery behaviour of the system is shown in Fig. 9 and these studies were divided into three time intervals. The first interval involved measuring the viscosity of the system at very low and continuous shear rate (0.001 s^{-1}) for 1000 s. Over this period of time, the viscosity decreased, indicating that microstructural reorganisation takes place at very low shear rate. The second interval measured the viscosity at comparatively high shear rates, namely 100, 1000, 1500 s^{-1}, for 100s and showed a dramatic drop in viscosity, as expected from the flow profile of the surfactant system in Fig. 8. Finally, in the third interval, the shear recovery is investigated by continuously monitoring the viscosity at low shear rate of 0.001 s^{-1} (as in *interval 3*) for 1 hour immediately after high shear. The shear recovery profile corroborates the thixotropy observed in Fig. 8: as soon as the shear rate decreases to 0.001 s^{-1} from *interval 2*, an immediate increase in viscosity takes place. It reaches lower values, however, than those of the end of *interval 1*. The magnitude of the viscosity jump scales (non-linearly) to the shear rate applied in the second interval and the higher the shear rate in *interval 2*, the higher the recovery viscosity measured in *interval 3*.

We next compare the flow profile for the mixture following shear in a Couette cell with that following extensional flow. The results are shown in Figure 9. Given the relatively low throughput of fluid processing in a microchannel, which would require collecting the sample volume needed for a rheology measurement in a timescale comparable with the fluid relaxation time, an alternative procedure was used. Extensional flow was applied by injection of the mixture through a needle of 0.5 mm diameter for 1.3 s, corresponding to an extension rate of 100 s^{-1} (and estimated wall shear 1900 s^{-1}). A short time delay ($\simeq$60 s) was necessary to setup and initiate measurement. Note that residence times for the extensional flow are approximately 1/100th of those experienced by the sheared sample in the Couette geometry, in line with the previously reported short 'processing' extensional sections of the microfluidic devices. Both 'shear' and 'extension' specimens were measured under the same conditions, monitored at a low shear rate of 0.001 s^{-1}, as shown in Figure 9. Clearly, the vis-

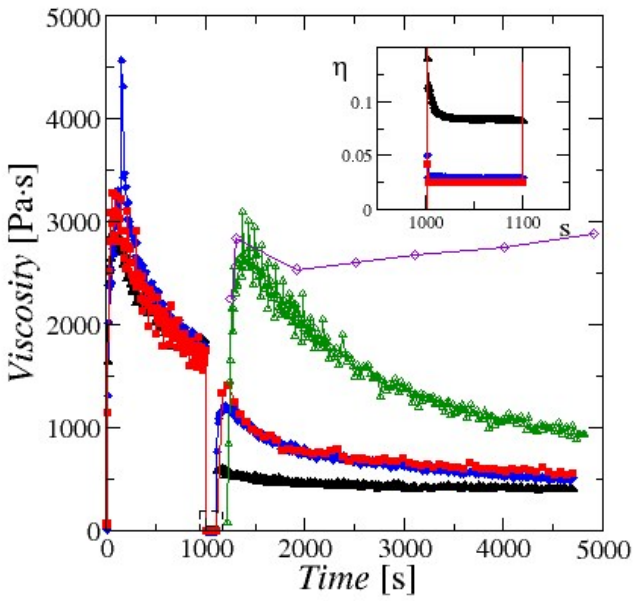

Fig. 9 Viscosity profiles (inset: close-up) of CTAC/Pentanol/Water measured in a Couette cell with three consecutive different intervals. Interval 1: at continuous low shear rate of $0.001 s^{-1}$ for 1000s; Interval 2: at continuous high shear rate (100 (▲), 1000 (♦), 1500 (■) s^{-1}) for 100s; Interval 3: at continuous low shear rate of $0.001 s^{-1}$ for 1h for samples sheared in interval 2. In interval 3, the recovered viscosity was also measured for a sample sheared into the Couette cell with high extension ($100 s^{-1}$) through a needle for 1.3s at continuous △ and discontinuous ◊ low shear rate of 0.001 s^{-1}.

cosity of the 'extensional' sample is significantly higher than that of the system sheared in the Couette cell at 1500 s^{-1}.

Two types of measurements were conducted, namely under continuous and discontinuous (very low) shear rate of 0.001 s^{-1} in order to investigate relaxation/recovery over time. By measuring 'discontinuously' (Fig. 9), i.e. only interrogating the viscosity every 500-1000 s, one obtains a more direct measurement of the recovery viscosity, preserving the microstructure and flow alignment caused by extensional flow. Such measurements clearly show that the viscosity remains constant or even *increases* over time, in contrast with the 'continuous' measurement, as well as the (Couette) shear measurement, where it decreases considerably.

Evidently, shear and extensional flow histories yield qualitatively different flow response and relaxation behaviour. These results relate directly to the microfluidics experiments **MC1** and **MC2/3** discussed above, which established that both structural order and *d*-spacing increased pronouncedly during extensional flow and again, subsequently, upon relaxation over 10's min. Our tentative mechanistic interpretation in terms of water molecules swelling the interlamellar spacing is in agreement with the current observations, as lamellar swelling (up to 10% in this case) and water removal from the matrix is expected to significantly increase viscosity.

4 Conclusion

Microfluidic processing of flow-responsive complex fluids, combined with online SAXS and microscopy, is shown to provide direct insight into their molecular and mesoscopic structure which can be further correlated with macroscopic performance measurements, including rheology. The micro-SAXS measurements require careful design and fabrication of compatible devices, in order to minimise background but ensure mechanical integrity. Further, spatio-temporal flow mapping over large distances (10's cm), relevant for flow 'processing', require the establishment of an accurate measurement grid of positions, that must be reproducible and stable over many hours. In this work, we have successfully implemented a simple PDMS-based approach that is suitable for a wide range of aqueous systems with sharp scattering features (e.g. liquid crystalline peaks). This approach is precise, low cost and allows rapid prototyping that is key for interrogating a variety of flow fields.

For the model system chosen of CTAC/pentanol/water, we are able to correlate flow type and magnitude to the resulting molecular structure, including the interlamellar *d*-spacing and orientation, as well as flow rheology. In summary, extensional flows result in highly oriented lamellar sheets that, over time, increase in *d*-spacing, upon a recovery process that is accompanied by a substantial viscosity increase. This is rationalised in terms of the incorporation of water molecules between lamellar sheets. Wall shear rate is also capable of increasing *d*-spacing but the effects are slower and more modest. The time scales of 'processing' are decoupled from those of structural rearrangement (or 'recovery') and are typically of ms-s and min-h timescales, respectively, depending on flow rates and geometry. During flow processing, in particular during a series of contraction-expansion flows **MC2**, an interplay between lamellar compression and structural relaxation takes place. Indeed, at sufficiently large flow velocity ($\geq$2 cms^{-1}), the lamellar spacing *d* approaches the quiescent value ($\simeq$59 Å) at the end of the 'processing' section. In this limit, water molecules are expelled upon compression and the short residence times do not allow 'swelling' to take place; lower velocities allow relaxation to occur during the 'processing' region. At high extensional rates, highly aligned lamellae structures assemble within flow constrictions, exhibiting minimal birefringence but sharp structural peaks. Following relaxation and a transient *d*-spacing increase, over much longer timescales (of the order of days), the *d*-spacing returns to the quiescent value of 59 Å indicating that such flow-induced structures are out-of-equilibrium but are relatively long-lived.

This study demonstrates that valuable insight on the flow-behaviour and thermodynamics of complex fluids can be gained from combining microfluidic and spatio-temporal SAXS, in addition to well-established microscopy and rheology. These results are important for the optimisation and manufacture of concentrated surfactant systems, with ubiquitous applications in the consumer goods industry, in terms of their rheological performance and metastability. From a fundamental perspective, this approach provides unprecedented opportunities to understanding non-equilibrium phenomena in non-Newtonian fluids and quantifying the effects of flow type and magnitude with the unique flexibility provided by microfluidic rapid prototyping.

5 Acknowledgements

We acknowledge EPSRC and Unilever for financial support (CASE/CNA05/63), the EPSRC for the platform grant EP/G00465X and the outward secondment of HPM to Unilever, and Diamond Light Source (Oxfordshire) for beamtime. We acknowledge Claire Pizzey, Marc Malfois (Diamond Light Source) and Him Cheng Wong (Imperial) for assistance during SAXS measurements, and George Wang (Imperial) for help with profilometry.

References

1 Y. Chevalier and T. Zemb, *Rep. Prog. Phys.*, 1990, **53**, 279–371.
2 R. G. Laughlin, *The aqueous phase behaviour of surfactants*, Elsevier Science London, 1996.
3 T. F. Tadros, *Applied Surfactants: Principles and Applications*, Elsevier, 2005.
4 T. Zemb and P. Lindner, *Neutrons, X-rays and Light. Scattering Methods Applied to Soft Condensed Matter*, Elsevier, 2002.
5 P. Partal, A. J. Kowalski, D. Machin, N. Kiratzis, M. G. Berni and C. J. Lawrence, *Langmuir*, 2001, **17**, 1331–1337.
6 V. Castelletto, P. Parras, I. W. Hamley, P. Baverback, J. Skov Pedersen and P. Panine, *Langmuir*, 2007, **23**, 6896–6902.
7 P. Herve, D. Roux, A.-M. Bellocq, F. Nallet and T. Gulik-Krzywicki, *Journal de Physique II*, 1993, **3**, 1255–1270.
8 P. Sierro and D. Roux, *Physical Review Letters*, 1997, **78**, 1496–1499.
9 P. Panizza, A. Colin, C. Coulon and D. Roux, *Eur. Phys. J. B*, 1998, **4**, 65–74.
10 W. Richtering, *Current Opinion In Colloid & Interface Science*, 2001, **6**, 446–450.
11 T. M. Squires and S. R. Quake, *Reviews of Modern Physics*, 2005, **77**, 977–1026.
12 S. D. Hudson, F. R. Phelan, M. D. Handler, J. T. Cabral, K. B. Migler and E. J. Amis, *Applied Physics Letters*, 2004, **85**, 335–337.
13 A. D. Stroock, S. K. W. Dertinger, A. Ajdari, I. Mezic, H. A. Stone and G. M. Whitesides, *Science*, 2002, **295**, 647–651.
14 H. A. Stone, A. D. Stroock and A. Ajdari, *Annual Review of Fluid Mechanics*, 2004, **36**, 381–411.
15 J. T. Cabral, S. D. Hudson, C. Harrison and J. F. Douglas, *Langmuir*, 2004, **20**, 10020–10029.
16 J. T. Cabral and S. D. Hudson, *Lab Chip*, 2006, **6**, 427–436.
17 E. Greaves and A. Manz, *Lab Chip*, 2005, **5**, 382–391.
18 H. P. Martin, N. J. Brooks, J. M. Seddon, N. J. Terrill, P. F. Luckham and J. T. Cabral, *Journal of Physics: Conference Series*, 2010, **247**, 012050.
19 L. Pollack, M. Tate, A. Finnefrock, C. Kalidas, S. Trotter, N. Darnton, L. Lurio, R. Austin, C. Batt, S. Gruner and S. Mochrie, *Phys. Rev. Lett.*, 2001, **86**, 4962–4965.
20 L. Pollack, *Biopolymers*, 2011, **95**, 543–549.
21 S. V. Kathuria, L. Guo, R. Graceffa, R. Barrea, R. P. Nobrega, C. R. Matthews, T. Irving, and O. Bilsel, *Biopolymers*, 2011, **95**, 550–558.
22 M. Trebbin, D. Steinhauser, J. Perlich, A. Buffet, S. V. Roth, W. Zimmermann, J. Thiele and S. Frster, *Proceedings of the National Academy of Sciences*, 2013, **110**, 6706–6711.
23 B. F. B. Silva, M. Zepeda-Rosales, N. Venkateswaran, B. J. Fletcher, L. G. Carter, T. Matsui, T. M. Weiss, J. Han, Y. Li, U. Olsson and C. R. Safinya, *Langmuir*, 2015, **31**, 4361–4371.
24 S. With, M. Trebbin, C. B. A. Bartz, C. Neuber, M. Dulle, S. Yu, S. V. Roth, H.-W. Schmidt and S. Frster, *Langmuir*, 2014, **30**, 12494–12502.
25 L. E. Rodd, J. J. Cooper-White, D. V. Boger and G. H. McKinley, *Journal of Non-Newtonian Fluid Mechanics*, 2007, **143**, 170–191.
26 J. A. Pathak and S. D. Hudson, *Macromolecules*, 2006, **39**, 8782–8792.
27 J. Penfold and I. Tucker, *J. Phys. Chem. B*, 2007, **111**, 9496–9503.
28 O. E. Shklyaev and A. Q. Shen, *Mechanics Research Communications*, 2009, **36**, 121–124.
29 M. Vasudevan, E. Buse, D. Lu, H. Krishna, R. Kalyanaraman, A. Q. Shen, B. Khomami and R. Sureshkumar, *Nat. Mater.*, 2010, **9**, 436–441.
30 M. Pasquali, *Nat. Mater.*, 2010, **9**, 381–382.
31 P. Cheung, N. Dubash and A. Q. Shen, *Soft Matter*, 2012, **8**, 2304–2309.
32 I. Grillo, *Current Opinion in Colloid & Interface Science*, 2009, **14**, 402 – 408.
33 K. A. Murthy and E. W. Kaler, *Coll. Polym. Sci.*, 1989, **267**, 330–335.
34 K. Fontell, A. Khan, B. Lindstrom, D. Maciejewska and S. Puangngern, *Coll. Polym. Sci.*, 1991, **269**, 727–742.
35 R. Makhloufi, E. Hirsch, S. Candau, W. Binanalimbele and R. Zana, *J. Phys. Chem.*, 1989, **93**, 8095–8101.
36 Y. N. Xia and G. M. Whitesides, *Angewandte Chemie-International Edition*, 1998, **37**, 551–575.
37 D. R. Reyes, D. Iossifidis, P. A. Auroux and A. Manz, *Anal. Chem.*, 2002, **74**, 2623–2636.
38 P. A. Auroux, D. Iossifidis, D. R. Reyes and A. Manz, *Analytical Chemistry*, 2002, **74**, 2637–2652.
39 T. Vilkner, D. Janasek and A. Manz, *Analytical Chemistry*, 2004, **76**, 3373–3385.
40 M. Unger, H. Chou, T. Thorsen, A. Scherer and S. Quake, *Science*, 2000, **288**, 113–116.
41 Y. Son, *Polymer*, 2007, **48**, 632–637.
42 J. Penfold, E. Staples, I. Tucker, P. Carroll, I. Clayton, J. S. Cowan, G. Lawton, S. Amin, A. Ferrante and N. Ruddock, *The Journal of Physical Chemistry B*, 2006, **110**, 1073–1082.
43 *The scattering length density for the components of the mixture is estimated to be* $\rho(H_2O)$*=9.46* 10^{-6} $Å^{-2}$, $\rho(CTAC)$*=9.38* 10^{-6} $Å^{-2}$, *and* $\rho(pentanol)$*=7.83* 10^{-6} $Å^{-2}$ *yielding limited SAXS contrast. Quadrupolar splitting NMR or contrast-variation neutron scattering would have to be employed, provided that H-D exchange occurs slowly compared to measurement timescales.*
44 V. Lutz-Bueno, J. Kohlbrecher and P. Fischer, *Journal of Non-Newtonian Fluid Mechanics*, 2015, **215**, 818.
45 C. G. Lopez, T. Watanabe, A. Martel, L. Porcar and J. T. Cabral, *Scientific Reports*, 2015, **5**, 7727.